A study of substitutional disorder in $Cr^{3+}$ : $CaYAlO_4$: I. Fluorescence line narrowing



1996 J. Phys.: Condens. Matter 8 3487

(http://iopscience.iop.org/0953-8984/8/19/023)

J. Phys.: Condens. Matter **8** (1996) 3487–3503. Printed in the UK

# A study of substitutional disorder in $Cr^{3+}$:$CaYAlO_4$: I. Fluorescence line narrowing

Mitsuo Yamaga†, Peter I Macfarlane‡, Keith Holliday‡, Brian Henderson‡, Nobuhiro Kodama§ and Yuka Inoue§

† Department of Physics, Faculty of General Education, Gifu University, Gifu 501-11, Japan
‡ Department of Physics and Applied Physics, University of Strathclyde, Glasgow G1 1XN, UK
§ Tosoh Corporation, Hayakawa, Ayase 252, Japan

Received 18 December 1995, in final form 21 February 1996

**Abstract.** A high-resolution study of the optical properties of $Cr^{3+}$-doped $CaYAlO_4$ is presented. Excitation into the usual $Cr^{3+}$ broad absorption bands produces fluorescence from a very broad $R_1$ line with a peak at 13 475 $cm^{-1}$ at 15 K. The $R_2$ line is observed at an energy 160 $cm^{-1}$ higher at temperatures above 100 K or by using excitation spectroscopy. The large broadening of the $^2E$ excited state is attributed to substitutional disorder at the $Ca^{2+}$ and $Y^{3+}$ sites on the basis of site selective excitation and fluorescence line narrowing measurements. Estimates of the distributions of octahedral and non-octahedral contributions to the crystal field are made and it is shown that the non-octahedral crystal field is dominant.

## 1. Introduction

The energy levels of transition metal ions in solids are primarily determined by the electron–electron interactions, described by the Racah parameters, and by the strength and symmetry of the crystal field. Transition metal ions prefer sites of approximately octahedral symmetry. The magnitude of the octahedral crystal field is characterized by 10Dq and is inversely proportional to $d^5$ in a point ion lattice theory, where $d$ is the distance between the central metal ion and its ligand ions [1]. In $CaYAlO_4$ (CYA), the crystal field splittings are expected to be much larger than in most oxides because the distance $d$ in CYA is small at about 0.19 nm. CYA crystals containing different dopants have been prepared as potential tuneable solid-state laser materials [2, 3]. The optical absorption and luminescence spectra of $Ti^{3+}$ and $V^{4+}$ in CYA crystals were observed to be broadened by the combined effects of the electron–phonon interaction and disorder associated with the random occupation of the $Ca^{2+}/Y^{3+}$ sites. A $Ca^{2+}/Y^{3+}$ composition ratio of 1:1 is maintained in the bulk CYA host crystal but statistical fluctuations occur locally [2, 3]. This is known as substitutional disorder.

Fluorescence from $Cr^{3+}$ in strong crystal field sites consists of a sharp zero-phonon line and its weak one-phonon sideband. In consequence, $Cr^{3+}$ ions in CYA are suitable spectroscopic probes of the substitutional disorder in this crystal. The present paper reports the results of the optical absorption, fluorescence, and fluorescence line narrowing studies of $Cr^{3+}$ in the disordered host lattice.

0953-8984/96/193487+17$19.50  

## 2. Crystal growth and experimental procedure

The crystal structure of $CaYAlO_4$ is shown in figure 1 and has the space group $I4/mmm(D_{4h}^{17})$ [4]. The lattice constants are $a = b = 0.364\,51$ nm and $c = 1.187\,43$ nm. The x-ray analysis of the crystal structure reveals $AlO_6$ octahedra centred on the $Al^{3+}$ ion but stretched along the $c$-axis such that the distances between $Al^{3+}$ and those $O^{2-}$ ions located along the $a$- and $c$-axes, respectively, are 0.1821 nm and 0.1992 nm. In consequence, the $AlO_6$ octahedral have tetragonal symmetry. Impurity $Cr^{3+}$ ions preferentially occupy $Al^{3+}$ sites in the crystal.

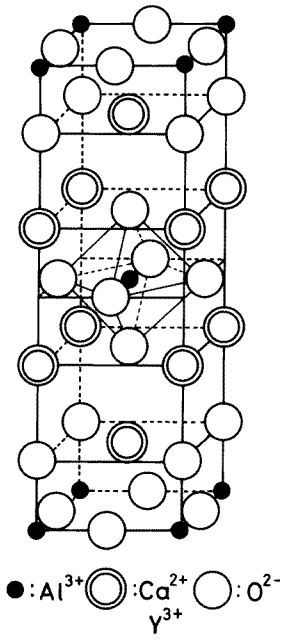


**Figure 1.** The structure of $CaYAlO_4$.

CYA single crystals doped with $Cr_2O_3$ at concentrations of $C = 0.1$, 0.5, and 2.0 mol% were grown in an argon gas atmosphere by the Czochralski technique from melts prepared in iridium crucibles with high-purity components $CaCO_3$(5 N):$Y_2O_3$(5 N):$Al_2O_3$(5 N) = 2:1:1. Pulling rates and seed rotation rates were 0.8–3.0 mm $h^{-1}$ and 3–5 rpm, respectively. The resulting boule was cut and polished into samples with approximate dimensions $4 \times 4 \times 4$ $mm^3$, the cut faces being normal to the $a$-, $b$- and $c$-axes, of the crystal.

Optical absorption spectra were measured at liquid nitrogen and room temperatures using a conventional double-beam spectrophotometer. The sample was mounted on a cold finger in a liquid nitrogen cryostat. Fluorescence was excited using a cw Spectra-Physics 2020-5 Ar ion laser, or a rhodamine 6G dye laser pumped by the Ar ion laser. For fluorescence line narrowing (FLN), narrow-line laser output was obtained from a single-mode Ti:sapphire ring laser pumped by the Ar ion laser. The cw laser excitation beam was mechanically chopped at a frequency of 3 kHz. In FLN measurements, fluorescence from the samples passes through a chopper with 180° phase delay, relative to that of the excitation beam, to suppress detection of scattered excitation light. Subsequently, the fluorescence signal is focused onto the entrance slit of a 1 m monochromator or as a parallel beam into a Fabry–

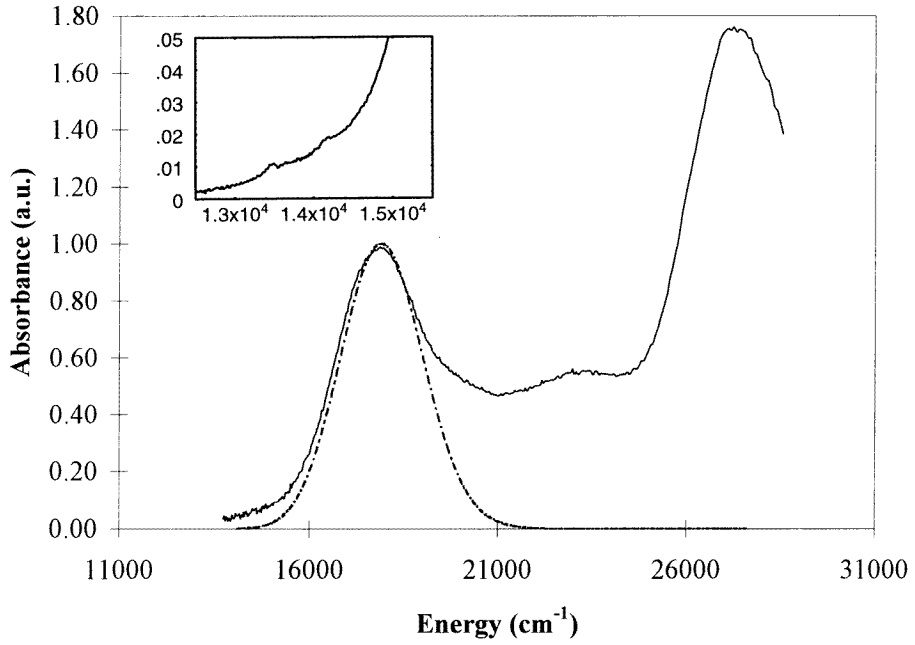


**Figure 2.** The unpolarized absorption spectrum of CYA at 77 K. The inset spectrum shows the $^4A_2 \rightarrow {}^2T_1$ and $^4A_2 \rightarrow {}^2E$ transitions. The dashed line is the spectrum simulated by equation (11).

Perot interferometer with 4 mm mirror separation corresponding to a maximum resolvable bandwidth of 0.05 $cm^{-1}$. The fluorescence was detected by a Hamamatsu Photonics R943-02 photomultiplier in single-photon-counting mode. The pulses were accumulated by a Stanford Research Systems SR400 counter. The excitation wavelength was measured using a Burleigh wavemeter. Lifetime measurements were carried out using a HeNe laser chopped mechanically at 50 Hz and an SR250 boxcar averager. Measurements of the temperature dependence of the fluorescence spectrum, the FLN spectrum, and the lifetime were made with the sample mounted on a cold finger in a cryorefrigerator in the range 15–300 K.

## 3. Results

### *3.1. Optical absorption spectra*

The optical absorption spectra of three CYA crystals containing 0.1, 0.5, and 2.0 mol% $Cr_2O_3$ have been measured at 77 and 300 K. As the Cr content of the CYA crystals increases, their colours change from violet to red. Figure 2 shows the low-temperature optical absorption spectrum of the violet-coloured Cr(0.5%):CYA sample. The two strong absorption bands which have peaks at 17 900 and 27 400 $cm^{-1}$ when measured at 77 K (and 17 650 and 27 100 at 300 K) are also observed in the R line excitation spectrum (figure 3) and these are assigned to the $^4A_2 \rightarrow {}^4T_2$ and $^4A_2 \rightarrow {}^4T_1$ ($t_2^2e$) transitions, respectively. The excitation spectrum also shows an additional band, beyond the range of the absorption spectrometer, that peaks at about 40 000 $cm^{-1}$. The precise peak is difficult to define due to the weak excitation power in this region but the band can be confidently assigned to the

transition from the $^4A_2$ to the higher $^4T_1$ ($t_2e^2$) state. The absorption spectrum contains an additional band at 23 000–24 000 $cm^{-1}$. In the most concentrated sample (2%), the additional band is strongest and has a peak absorption at 23 250 $cm^{-1}$. This band is much weaker in the excitation spectrum for R-line fluorescence however and is probably not related to the main $Cr^{3+}$ centre discussed in this paper.

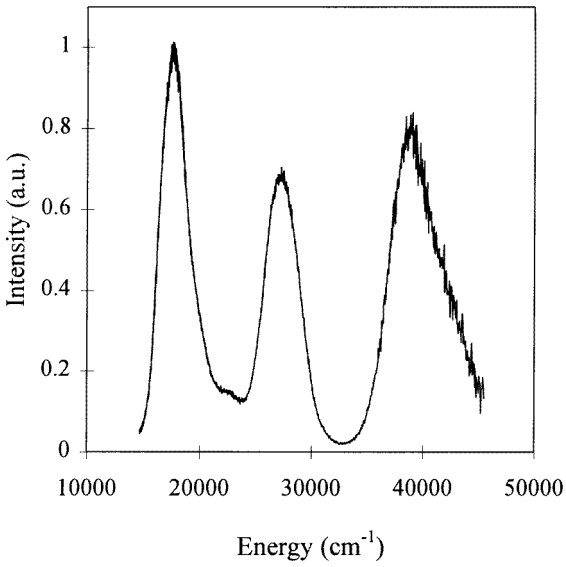


**Figure 3.** The room-temperature, unpolarized excitation spectrum of CYA, obtained by monitoring the R-line luminescence at 13 475 $cm^{-1}$.

As is expected in a tetragonally symmetric crystal the absorption spectra are strongly polarized. The intensities of the $^4A_2 \rightarrow {}^4T_2$, $^4T_1$ absorption bands measured with light polarized along the *c*-axis ($E \| \langle 001 \rangle$) are approximately twice the intensities measured with light polarized along the *a*- and *b*-axes of the crystal ($E \| \langle 100 \rangle$, $\langle 010 \rangle$). These observed ratios of the polarized intensities cannot be explained by a simple tetragonal distortion along the *c*-axis. Such a distortion is expected to lead to polarized intensities $A_{\langle 100 \rangle}$:$A_{\langle 010 \rangle}$:$A_{\langle 001 \rangle} = 1{:}1{:}0$ [5]. The polarization strongly depends on the symmetry of the $CrO_6$ octahedra, as revealed by electron spin resonance (ESR) experiments [3]. A detailed analysis of the polarization will be discussed in the second paper of this pair, combined with ESR results [6].

The inset in figure 2 shows three relatively sharp but weak features at 13 470, 13 630 and 14 140 $cm^{-1}$ and these are ascribed to $Cr^{3+}$ absorption to the split $^2E$ states and the $^2T_1$ state respectively. This is confirmed by resonantly exciting them, which results in R-line luminescence in all cases (see below). It is assumed that the feature at 14 140 $cm^{-1}$ is not the $^4A_2 \rightarrow {}^4T_2$ zero-phonon line because the magnitude of the Huang–Rhys factor is large ($S \sim 7$) and the intensity of the $^4A_2 \rightarrow {}^4T_2$ zero-phonon line relative to the total intensity of the absorption band is proportional to $e^{-S}$; also, the distribution of 10Dq (discussed below) would suggest that the weak $^4A_2 \rightarrow {}^4T_2$ zero-phonon line is broadened.

### *3.2. Photoluminescence and lifetime of the $R_1$ line*

Figure 4 shows the fluorescence spectra of the Cr(0.1%):CYA sample measured at 15 K and excited in the energy range 16 000–19 500 $cm^{-1}$ of the $^4A_2 \rightarrow {}^4T_2$ absorption band. The fluorescence consists of a $Cr^{3+}$ $R_1$ line and its phonon-assisted sideband. The linewidth of the $R_1$ line ($\sim$ 100 $cm^{-1}$) is much greater than those in some Gd garnets (10–30 $cm^{-1}$) [7] and other disordered crystals (50–65 $cm^{-1}$) [8, 9], but less than those in glasses (200–250 $cm^{-1}$) [10]. Figure 5 shows the relationship between the excitation energy and the photon energy at the peak of the $R_1$ line. Initially, the peak energy increases gradually as the excitation energy increases but then remains approximately constant at excitation energies above $\sim$ 19 000 $cm^{-1}$.

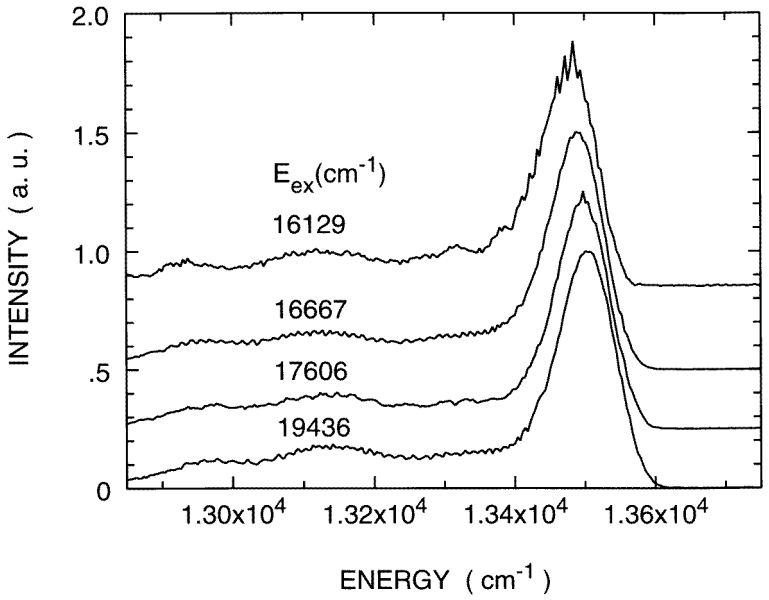


**Figure 4.** The R-line and Stokes sideband luminescence of CYA excited at various wavelengths within the $^4A_2 \rightarrow {}^4T_2$ absorption band measured at 15 K.

Figure 6 shows the temperature dependence of the $R_1$-line fluorescence spectrum in Cr(0.1%):CYA excited with the 633 nm output of a HeNe laser. The fluorescence intensity gradually increases and the width increases as temperature increases. An additional line at 13 620 $cm^{-1}$ which appears above $T \sim 100$ K is the zero-phonon $R_2$ line. This assignment has been confirmed by the low-temperature excitation spectrum monitoring fluorescence at about 13 300 $cm^{-1}$, corresponding to the one-phonon emission band of the $R_1$ line (see below). Two peaks of similar widths and intensities are observed corresponding to absorption into the $R_1$ and $R_2$ lines. The energy separation between the $R_1$ and $R_2$ lines of about 160 $cm^{-1}$ is much larger than the R-line separation ($\sim$ 40 $cm^{-1}$) in garnet crystals [7] but is comparable to that (137 $cm^{-1}$) in LSGO crystals [8]. A large R-line splitting is expected for $Cr^{3+}$ ions in strongly tetragonally distorted oxygen octahedra such as in CYA.

The temperature dependences of the integrated fluorescence intensities excited with the 633 nm HeNe and 488 nm $Ar^+$ laser lines are shown in figure 7(*a*). The intensity for excitation with the 633 nm laser line increases gradually above 70 K. In contrast, the

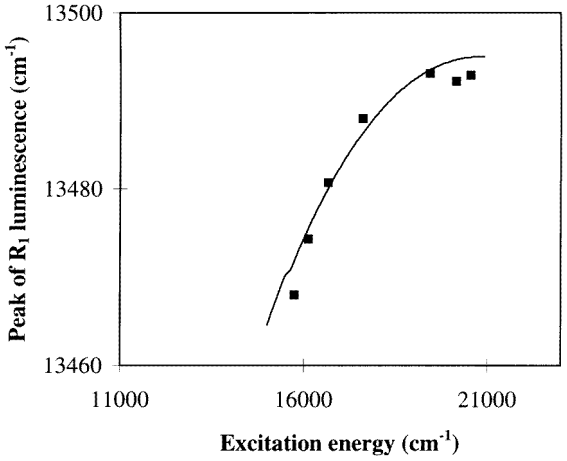


**Figure 5.** The peak position of the R-line luminescence plotted against excitation energy (symbols). The solid line is the simulated dependence, from equations (12) and (14).

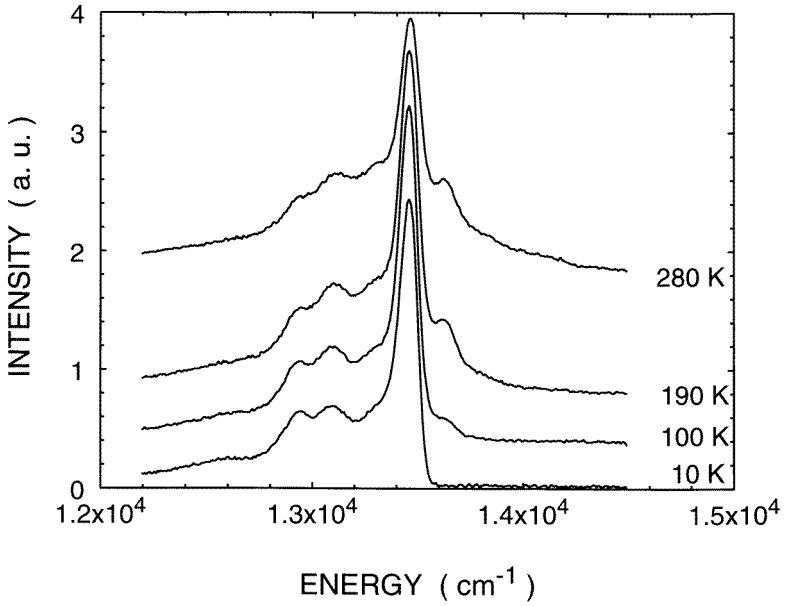


**Figure 6.** The temperature dependence of the R-line luminescence.

spectrum excited with the 488 nm laser line has almost constant intensity in the temperature range 15–300 K. The increase of the intensity above 70 K for excitation at 15 800 $cm^{-1}$ (633 nm) is attributed to enhancement of the absorption coefficient at 15 800 $cm^{-1}$ as a consequence of the $^4T_2$ absorption band shifting to lower energy with increasing temperature due to thermal expansion of the crystal.

The lifetime of the $R_1$ line detected at 13 466 $cm^{-1}$ during 15 800 $cm^{-1}$ excitation was measured in range 15–300 K. The lifetime gradually increases from a low-temperature value

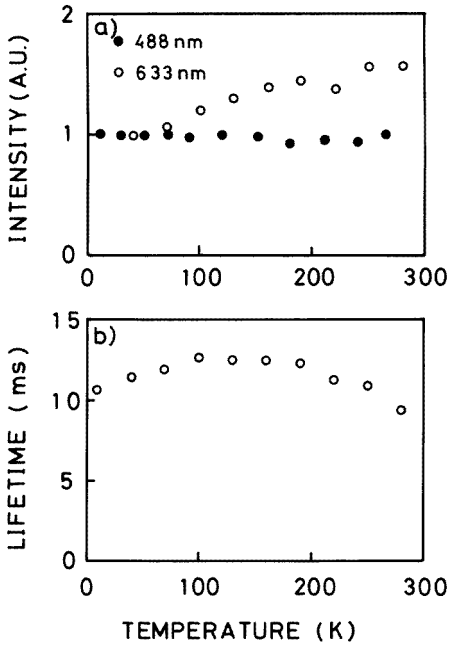


**Figure 7.** (*a*) Temperature dependences of the integrated luminescence intensity. (*b*) Temperature dependence of the luminescence decay time.

of 10.7 ms to a maximum value at $\sim$ 150 K of 12.7 ms, gradually decreasing above this temperature, as shown in figure 7(*b*).

### *3.3. Fluorescence line narrowing*

In order to investigate the substitutional disorder in CYA, FLN spectra were recorded at low temperatures. The FLN spectra were detected using a 1 m monochromator that determined the resolution of the measurements. The slit width varied in order to obtain detectable FLN signals across the R line. The resolution was 8 $cm^{-1}$ in the wings of the R line where signals are weak, but less close to its peak where the slit width could be reduced. Figure 8(*a*) shows the FLN spectra in the excitation energy range 13 386–13 480 $cm^{-1}$, compared with the $R_1$ line excited by all lines from an $Ar^+$ ion laser. The FLN spectra are composed of an intense resonant line at the excitation energy and fairly weak fluorescence in the low-energy range 12 800–13 350 $cm^{-1}$. The FLN spectrum excited at 13 480 $cm^{-1}$, close to the peak energy of the $R_1$ line, is shown with non-resonant features magnified by a factor of 10. The non-resonant features are seen to be coincident with the phonon structure of the fluorescence excited by all lines from the Ar ion laser.

Figure 8(*b*) shows resonant lines excited at more than 13 500 $cm^{-1}$ accompanied by relatively intense and broad non-resonant lines. This is quite different from the phonon structure of the FLN spectra in figure 8(*a*). As the excitation energy increases, the intensity of the resonant line decreases compared with that of the broad non-resonant line. This non-resonant line is assigned to be the $R_1$-line fluorescence caused by excitation of the upper $^2E$ excited electronic state corresponding to the $R_2$ line.

Figure 9 shows the relationship between the peak energy of the non-resonant line ($R_1$

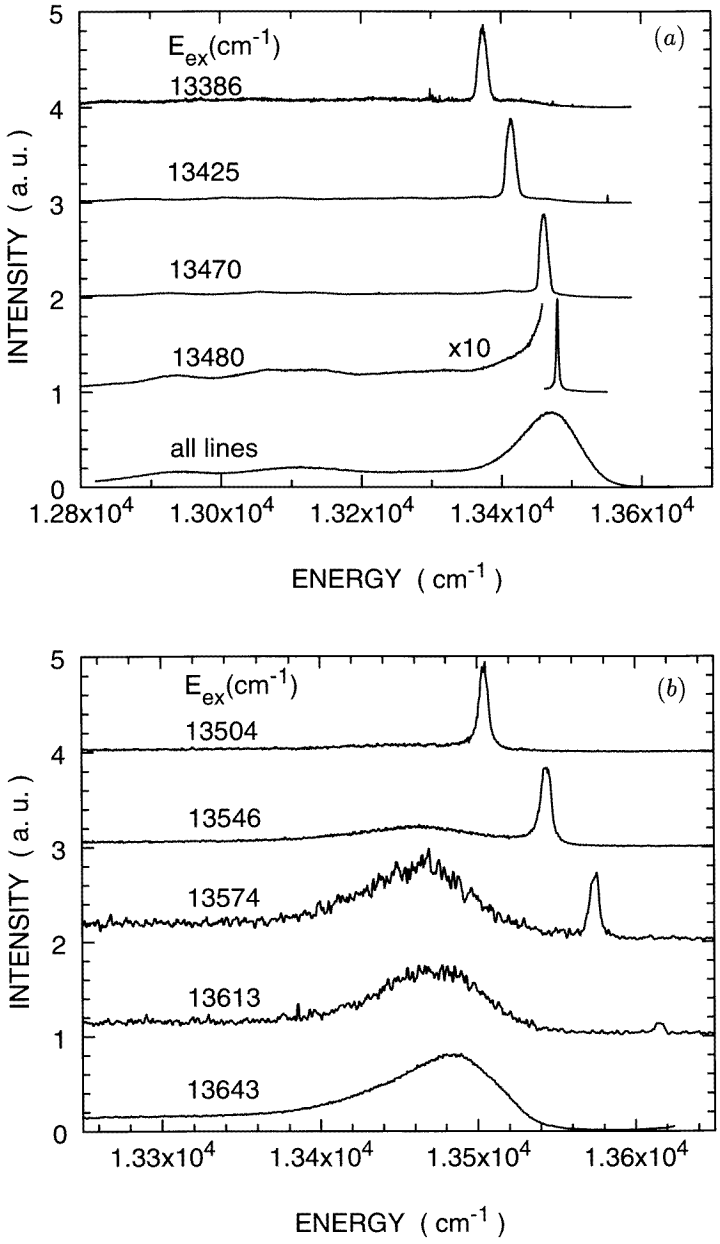


**Figure 8.** (*a*) Selected FLN spectra of CYA excited resonantly within the $R_1$ line by a single-mode Ti:sapphire laser. The inhomogeneously broadened spectrum excited by all lines of an argon ion laser is the lowest spectrum. (*b*) FLN spectra of CYA excited in the $R_2$ line.

line) in figure 8(*b*) and the excitation energy. The peak energy increases as the excitation energy increases, linearly above 13 580 $cm^{-1}$ and at a slower rate below 13 580 $cm^{-1}$. The separation between excitation and the peak fluorescence of these lines varies between 70 and 180 $cm^{-1}$, consistent with the R-line splitting of 160 $cm^{-1}$ obtained from the

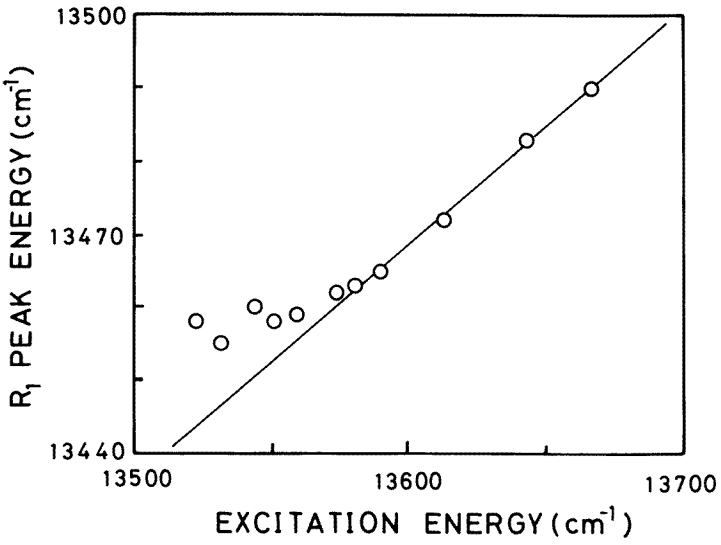


**Figure 9.** The peak of the $R_1$ luminescence for various excitation energies within the $R_2$ line.

higher-temperature $Cr^{3+}$ fluorescence.

Figure 10 shows the intensity of the FLN resonant lines as a function of the excitation energy without any change in the other experimental conditions. In comparison with the fluorescence spectrum excited by the $Ar^+$ ion laser, the intensity spectrum shows no overlap between the $R_1$-line spectrum and its one-phonon sideband. This spectrum reflects directly the distribution of the lower $^2E$ excited electronic energy level. Figure 10 also shows an excitation spectrum of the two $^4A_2 \rightarrow {}^2E$ transitions produced by removing some of the internal optics from the Ti:sapphire laser and rotating the birefringent filter at a constant rate. The spectrum is somewhat noisy due to mode hops of the laser but the widths of the lines and the splitting (160 $cm^{-1}$) are consistent with data taken using other methods.

Figure 11 shows an FLN spectrum excited at 13 481 $cm^{-1}$ and detected via a Fabry–Perot interferometer. The width of the resonant FLN line is less than 0.1 $cm^{-1}$, this being the limit of resolution set by the Fabry–Perot interferometer. The satellite lines in figure 11 are separated by $\sim 0.24$ $cm^{-1}$ from the central resonant line. Figure 12 plots this energy separation as a function of the excitation energy. The separation decreases linearly with increasing excitation energy. This high-resolution FLN spectrum is very similar to those observed for $Cr^{3+}$ in ruby [11], and in gallogermanates [9], where the satellite lines are due to the $^4A_2$ ground state splitting. The measured separation of the satellite FLN lines ($\sim 0.25$ $cm^{-1}$) in CYA is consistent with the zero-field splittings of the $^4A_2$ ground states of different $Cr^{3+}$ centres in CYA obtained from ESR measurements [6]. In the ESR measurements a number of centres have been identified, the least populated of which have smaller ground state splittings than the resolution of the Fabry–Perot etalon used here. The two dominant centres have ground state splittings of greater than 0.1 $cm^{-1}$, one of which corresponds very well with the measured splittings shown in figure 12 and the other of which is about half of this. The latter splitting is on the limit of resolution of the Fabry–Perot etalon and cannot be quantified here but does explain why the non-resonant features in figure 11 have the appearance of a plateau due to the overlap of the resonant and two pairs of non-resonant features.

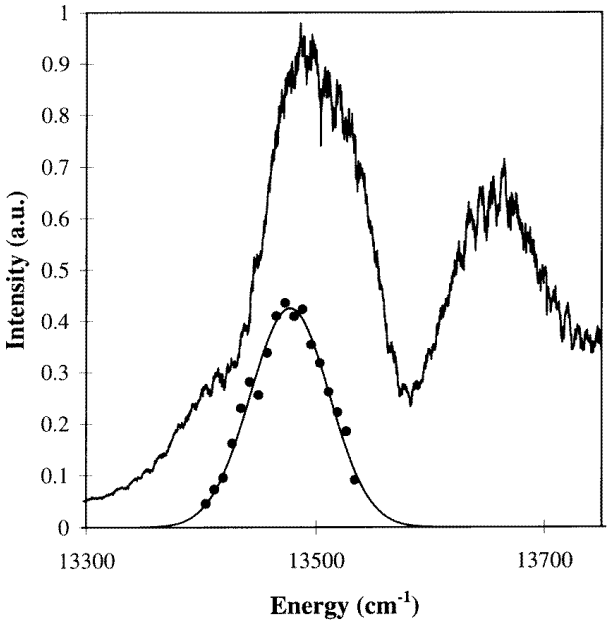


**Figure 10.** The excitation spectrum of the $^4A_2 \rightarrow {}^2E$ split transition detecting fluorescence in the R-line phonon sideband at 13 100 $cm^{-1}$ (upper trace). The intensity of the resonant components of FLN spectra recorded under constant experimental conditions are plotted as circles and fitted to a Gaussian with a standard deviation of 35 $cm^{-1}$.

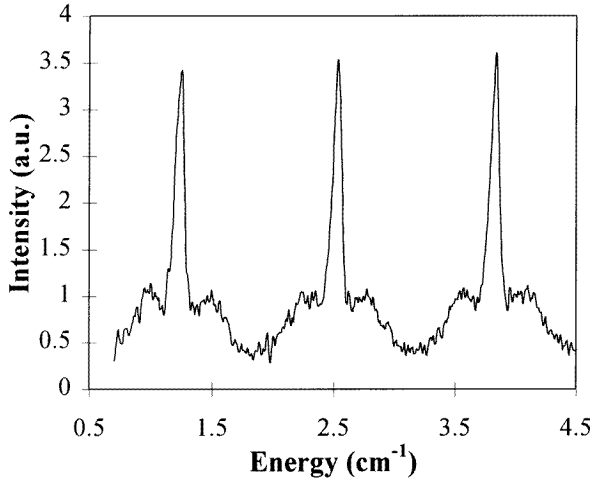


**Figure 11.** Resonantly excited $R_1$ luminescence dispersed in a Fabry–Perot etalon, showing three consecutive transmission orders. The separation of each side lobe from the central peak is the ground state splitting.

## 4. Discussion

### *4.1. Crystal field and Racah parameters*

In order to determine the mechanisms that cause inhomogeneous broadening it is necessary to make calculations using the crystal field and Racah parameters. The absorption and

excitation spectra (figures 2 and 3) with the peak position of the R-line luminescence allow the crystal field and Racah parameters to be calculated by diagonalizing the relevant matrices for these term energies [1]. 10Dq is the energy of the peak of the $^4A_2 \rightarrow {}^4T_2$ absorption band, giving Dq = 1790 $cm^{-1}$. Conventionally, the Racah *B* parameter is obtained from the separation of the peaks of the $^4A_2 \rightarrow {}^4T_1$ and $^4A_2 \rightarrow {}^4T_2$ absorption bands. These energies are 27 400 $cm^{-1}$ and 17 900 $cm^{-1}$ respectively. The Racah *B* parameter is obtained by diagonalizing the matrix for the $^4T_1$ terms. This gives the energy of the $^4T_1$ level relative to the ground state. From this, *B* is calculated to be 1100 $cm^{-1}$, which may be used to calculate the magnitude of the *C* parameter from the R-line energy using the matrix for the $^2E$ levels. The result is $C = 1760$ $cm^{-1}$. Comparison with all known data for $Cr^{3+}$-doped hosts [12] shows that 1100 $cm^{-1}$ is an extraordinarily large value for the *B* parameter; indeed it is larger than the free ion value [13]. In comparison, *C* is much smaller than is typical. The nephelauxetic effect reduces the Racah parameters of ions in solids from their free ion values, essentially due to covalency effects [14]. A Racah parameter that is larger than the free ion value is difficult to account for, especially in a host with a strong crystal field where the overlap of ligand and $Cr^{3+}$ electron orbitals would be expected to be great. These values are regarded as unreasonable.

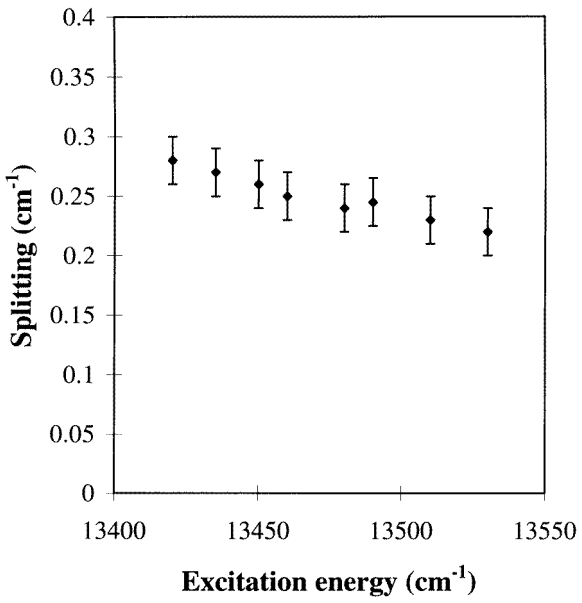


**Figure 12.** The variation of the ground state splitting of CYA as a function of the excitation energy.

If instead the Racah *B* and *C* parameters are obtained by simultaneously diagonalizing the energy matrices of the $^2E$ and the $^2T_1$ states to fit the R-line energy (13 475 $cm^{-1}$) and the energy of the small peaks near 14 100 $cm^{-1}$ in the absorption spectrum, which are assigned to the $^4A_2 \rightarrow {}^4T_1$ transition, the best fit obtained for $B = 705$ $cm^{-1}$ and $C = 2750$ $cm^{-1}$. The Racah parameters are now quite typical [12].

Calculating the energy of the $^4A_2 \rightarrow {}^4T_1$ band peak using $B = 705$ $cm^{-1}$ gives 24 700 $cm^{-1}$. This is 2300 $cm^{-1}$ lower in energy than the $^4A_2 \rightarrow {}^4T_1$ band observed in the absorption and excitation spectra (figures 2 and 3). Although there is no explanation

of why the value for $B$ of 705 $cm^{-1}$ does not fit the data of the $^4A_2 \rightarrow {}^4T_1$ lower band it fits the data of the $^4A_2 \rightarrow {}^4T_1$ upper band. Therefore, the Racah parameters derived from the energies of the R-line and $^4A_2 \rightarrow {}^2T_1$ transitions are assumed to be reliable and will be used in subsequent analysis.

### *4.2. Inhomogeneous broadening of the R lines*

The broadening of optical transitions of impurities in solids is often considered to be induced simply by a distribution in the strength of the octahedral component of the crystal field. However, it has been shown that the inhomogeneous broadening of optical transitions in the substitutionally disordered crystals $Ca_3Ga_2Ge_4O_{14}$ and $Sr_3Ga_2Ge_4O_{14}$ is dominated by the variation in distortions to the octahedral crystal field [9]. Similar behaviour has been observed in organochromic complexes [15]. More unusually, the electrostatic influence of near-neighbour impurity ions was shown not to account for the broadening of $Cr^{3+}$ optical transitions in $LiNbO_3$ and the mechanism was ascribed to variation in the electron–electron interaction strength, referred to as nephelauxetic inhomogeneous broadening [16].

It is shown below that it is not necessary to consider the contribution of nephelauxetic inhomogeneous broadening to explain the large broadening of the R lines in the case of $Cr^{3+}$:CYA. Three sets of experimental data are used to independently extrapolate the contributions of the octahedral and non-octahedral contributions to the broadening. Distributions of these contributions respectively cause the centre energy and splitting of the $^2E$ state to vary. The distribution function of the centre of gravity of the energy of the $^2E$ state as a function of energy, $x$ is assumed to be approximated by a Gaussian,

$$P_{oct}(x) = (1/\sqrt{2\pi}\sigma_{oct}) \exp[-(x - x_0)^2/2\sigma_{oct}^2] \tag{1a}$$

where $x_0$ is the centre energy of maximum probability and $\sigma_{oct}$ is the standard deviation of the distribution. The distribution function of the splitting, $E$, between the lower and upper $^2E$ excited states is assumed to be approximately represented by a second Gaussian,

$$P_{non}(E) = (1/\sqrt{2\pi}\sigma_{non}) \exp[-(E - \Delta_0)^2/2\sigma_{non}^2] \tag{1b}$$

where $\Delta_0$ is the splitting of maximum probability and $\sigma_{non}$ is the standard deviation of the distribution. The distribution functions of the lower and upper energy levels of the $^2E$ excited state, being $x - 1/2E$ and $x + 1/2E$, respectively, are convolutions of these distribution functions, i.e.

$$P_E^l(x) = \int_0^\infty P_{non}(E) P_{oct}(x + \tfrac{1}{2}E)\, dE. \tag{2a}$$

$$P_E^u(x) = \int_0^\infty P_{non}(E) P_{oct}(x - \tfrac{1}{2}E)\, dE. \tag{2b}$$

Both $P_{non}$ and $P_{oct}$ are assumed to be Gaussians and so the distributions that result from the convolutions will also be Gaussian with a standard deviation of $\sqrt{\sigma_{oct}^2 + (\sigma_{non}/2)^2}$ for both functions.

*4.2.1. Analysis of $R_1$ fluorescence due to $R_2$ excitation.* Figure 10 shows the intensities of the resonant FLN lines as a function of excitation energy together with a fit to the distribution function $P_E^l(x)$. The solid curve in figure 10 is calculated using the function $P_E^l(x)$ with parameters $x_0 - \frac{1}{2}\Delta_0 = 13\,580$ $cm^{-1}$ and $\sqrt{\sigma_{oct}^2 + (\sigma_{non}/2)^2} = 35$ $cm^{-1}$.

The distribution function of the lower $^2$E excited state as a function of the energy $x$ after relaxation from the upper $^2$E excited state energy levels is calculated to be given by

$$f_{u\to l}(x, E_{ex}) = \int_{-\infty}^{\infty} P_{non}(E_{ex} - x) P_{oct}(\tfrac{1}{2}(E_{ex} + x) - \omega) I(\omega)\, \mathrm{d}\omega \tag{3}$$

where the intrinsic lineshape is given by $I(\omega)$. The intrinsic lineshape function is a Lorentzian with a standard deviation determined by the homogeneous linewidth. This is likely to be very small on the scale of the inhomogeneous broadening in this material and is therefore taken to be a delta function, effectively disappearing from the calculation.

The reproduction function $f_{u\to l}(x, E_{ex})$ is analytically given by a Gaussian with a centre energy $x_l$ and width $\sigma_l$ as given by

$$x_l = [\sigma_{non}^2(2x_0 - \Delta_0) + (4\sigma_{oct}^2 - \sigma_{non}^2)(E_{ex} - \Delta_0)]/(4\sigma_{oct}^2 + \sigma_{non}^2) \tag{4}$$

$$1/\sigma_l^2 = 1/4\sigma_{oct}^2 + 1/\sigma_{non}^2. \tag{5}$$

The value of $\Delta_0$ in equation (4) is found to be 160 cm$^{-1}$ from figure 10. The gradient of the peak energy of the non-resonant $R_1$ line versus excitation energy, $E_{ex}$, which is obtained to be $\sim$ 0.33 from figure 9, is approximately equal to $(4\sigma_{oct}^2 - \sigma_{non}^2)/(4\sigma_{oct}^2 + \sigma_{non}^2)$ in equation (4). The value of $\sqrt{\sigma_{oct}^2 + (\sigma_{non}/2)^2}$ is 35 cm$^{-1}$ as stated above. The parameters of interest, the values of $\sigma_{oct}$ and $\sigma_{non}$ are thus calculated to be 25 cm$^{-1}$ and 49 cm$^{-1}$, respectively.

*4.2.2. Extrapolation from ground state splittings.* The ground state splitting, $\Delta_G$, due to a tetragonal distortion is approximately given by the expression

$$\Delta_G = -1.69 \times 10^{-9}\zeta^2\mu - 2.25 \times 10^{-9}\zeta^2\delta \tag{6}$$

where $\delta$ and $\mu$ are parameters which define the tetragonal component of the crystal field and $\zeta$ is the spin–orbit coupling parameter [17]. The numerical constants in equation (6) are combinations of the crystal field parameters obtained in subsection 4.1. An estimate of $\zeta$ can be obtained from the change in the $g$-factor caused by the effect of spin–orbit coupling, $g = 2.0023$, using the expression [18]

$$\zeta = (30\mathrm{Dq}/8)(g - 2.0023). \tag{7}$$

The $g$-factor has been measured to be 1.983 in $Cr^{3+}$:CYA [6], giving a value of 127 cm$^{-1}$ for $\zeta$. The expression for the $^2$E splitting, $\Delta_E$, due to a tetragonal crystal field is a function of the same parameters [17]:

$$\Delta_E = (-0.028 - 7.13 \times 10^{-8}\zeta^2)\mu + (0.063 - 9.51 \times 10^{-8}\zeta^2)\delta. \tag{8}$$

The tetragonal field parameters can be determined from the measured values of the ground and excited state splittings (0.24 cm$^{-1}$ and 160 cm$^{-1}$ respectively): $\delta$ is calculated as 2513 cm$^{-1}$ and $\mu$ is $-391$ cm$^{-1}$.

The measured variation of the ground state splitting in CYA (figure 12) implies that there is also a distribution of excited state splittings. In a point ion calculation, the parameter is found to decrease approximately four times as fast as $\delta$ increases for a tetragonal distortion varied by uniaxial stress [19]. It is thus possible, combining this result with equations (6) and (8), to obtain approximately the variation of excited state splittings, $\Delta_{\Delta E}$, from the measurement of the variation of ground state splittings, $\Delta_{\Delta G}$, assuming $\delta$ and $\mu$ are so related:

$$\Delta_{\Delta E}/\Delta_{\Delta G} \cong \{-4(-0.028 - 7.13 \times 10^{-8}\zeta^2) + (0.063 - 9.51 \times 10^{-8}\zeta^2)\} \times([(4 \times 1.69 \times 10^{-9}\zeta^2) - 2.25 \times 10^{-9}\zeta^2])^{-1}. \tag{9}$$

From this equation it is calculated that for a given variation of ground state splitting, the variation of the excited state splitting should be $\sim$ 2400 times as great. The observed variation of 0.06 $cm^{-1}$ for excitation energies between 13 420 and 13 530 $cm^{-1}$ implies that the excited state splitting should vary by 140 $cm^{-1}$ for the same excitation energies. The slope of the plot in figure 12 is $5.5 \times 10^{-4}$ and this may be extrapolated to the excited state, again by multiplying by the factor 2400. Clearly, the slope of the variation of the excited state splitting, 1.32, as extrapolated to the excited state, indicates the variation in the non-octahedral contribution to the broadening of the R lines and the standard deviation of the distribution of excited state splittings, $\sigma_{non}$, is estimated to be 56 $cm^{-1}$ using the same procedure that has been outlined in detail previously (see figure 6 in [9]). The standard deviation of the distribution of centre energies, $\sigma_{oct}$, is calculated to be 20 $cm^{-1}$ using the expression $\sqrt{\sigma_{oct}^2 + (\sigma_{non}/2)^2} = 35$ $cm^{-1}$ used in subsection 4.2.1.

*4.2.3. Analysis of $R_1$ fluorescence due to $^4T_2$ excitation.* As the energy separation of the $^4A_2$ and $^4T_2$ states is given simply by the strength of the octahedral crystal field, 10Dq, it is possible to independently derive parameters that describe the distributions of 10Dq and the Huang–Rhys parameter, $S$, from an analysis of the shift of the R-line fluorescence peak as a function of the energy of excitation in the $^4A_2 \rightarrow {}^4T_2$ absorption band. As the laser is tuned to lower energy, the contribution of weaker crystal field sites will increase. However, the proportion of sites excited by the laser can be affected by variation in the Huang–Rhys factor. It is necessary to consider both effects in the analysis of the spectra.

As in [9], and indicated by figure 10, it will be assumed that Gaussian distributions of 10Dq and the electron lattice coupling energy $S\bar{h}\omega$, exist in CYA, and a linear relationship between the minimum of the $^4T_2$ potential and the electron–lattice coupling energy will be assumed. Thus for the $i$th site

$$S_i\bar{h}\omega = S_0\bar{h}\omega - (E_i - E_0)K \tag{10}$$

where $S_0\bar{h}\omega$ is the mean electron lattice coupling energy and $E_0$ is the mean $^4T_2$ minimum potential energy relative to the ground state. The parameter $K$ is a constant, the value of which describes to some extent the influence of the lower-symmetry field. When $K = 0$, all variation in the crystal field is due to the octahedral contribution whereas when $K = 1$ the crystal field variation is due exclusively to the non-octahedral distortion. All other cases correspond to situations where there is a variation in both symmetries. A more physical interpretation of this behaviour is simply that reduction in the local symmetry of the $Cr^{3+}$ ion causes $S$ to increase through stronger coupling to non-symmetric vibrational modes. Strictly speaking this should be represented by a multi-dimensional configuration coordinate diagram but here, as in [9], a single coordinate is used to represent the overall coupling.

The $^4A_2 \rightarrow {}^4T_2$ absorption band of each site is assumed to be described by a Pekarian function, so that the absorption shape of site $i$ is

$$I_i(E) = I_0 \sum_m \frac{e^{-s_i} S_i^m}{m!} \delta(E - E_i - m\bar{h}\omega) \tag{11}$$

where $m$ refers to the phonon progression and $S_i$ and $E_i$ are respectively the minimum energy of the $^4T_2$ potential and the Huang–Rhys factor of the $i$th site. The density of excited states in 10Dq, $P$(10Dq), excited by monochromatic radiation of energy $E_{ex}$ is then given by

$$P(10\text{Dq}) = \sum_i I_i(E_{ex})\delta(10\text{Dq} - 10\text{Dq}_i) \tag{12}$$

where $10Dq_i$ is the peak of the absorption band relating to site $i$. $E_0$ and $S_0\bar{h}\omega$ are related by

$$E_0 = 10Dq_0 - S_0\bar{h}\omega \tag{13}$$

where $10Dq_0$ is the energy of the peak of the $^4A_2 \rightarrow {}^4T_2$ absorption band. The major part of the distribution of $^4T_2$ minima must be $\sim 1500$ cm$^{-1}$ greater than the R-line energy to account for the long lifetime of the $^2E$ states.

**Table 1.** The parameters used to fit the shift of fluorescence of the R lines as a function of excitation energy in the $^4T_2$ band where $\sigma$ denotes the standard deviation of the quantities that follow in brackets as identified in subsection 4.2.3.

| Parameter | Value |
|---|---|
| $S_0$ | 7.0 |
| $E_0$ | 15 850 cm$^{-1}$ |
| $\sigma(E_i)$ | 795 cm$^{-1}$ |
| $\sigma(S\bar{h}\omega)$ | 302 cm$^{-1}$ |
| $\sigma(P_{oct})$ | 493 cm$^{-1}$ |
| $K$ | 0.38 |

Equation (12) allows the distribution of sites excited by monochromatic radiation to be calculated, each site being characterized by a particular value of 10Dq. The problem then is how to map the distribution of 10Dq given by equation (12) onto the distribution of R-line energies. For the conditions $3 < C/B < 6$ and $1.5 < Dq/B < 3$, the energy of the R line is given to within 0.5% accuracy by [20]

$$E(^2E) = 3.05C + 7.9B - 1.8B^2/Dq. \tag{14}$$

However, it is noted that the Racah parameters are properly described as functions of 10Dq if the variation of the crystal field alters the overlap of the ligand ion and $Cr^{3+}$ electron orbitals (the nephelauxetic effect). It is arguable that because the R line shifts to lower energy as the density of weaker field sites excited is increased then the effect of reduction of 10Dq dominates any associated increase of the Racah parameters. Therefore assuming constant values of $B$ and $C$, enumerated above, the densities of states of 10Dq will be related to the R line by equation (14). The phonon energy, $\bar{h}\omega$, is assumed to be 350 cm$^{-1}$, corresponding to the strongest peak in the Stokes sideband of the R-line luminescence spectrum. The distribution of 10Dq is treated as a free parameter and adjusted for best fitting. The parameters of the model are listed in table 1. The simulated dependence of the R-line peak energy on excitation energy using these parameters is shown in figure 5 and the simulated $^4A_2 \rightarrow {}^4T_2$ absorption band is shown in figure 2. Both are in good agreement with experiment. For the parameters that give the best fit, the calculated standard deviation of the R line due to the influence of variations in the octahedral crystal field, $\sigma_{oct}$, is 15 cm$^{-1}$ and the standard deviation of the splittings of the R lines, $\sigma_{non}$, is calculated to be 55 cm$^{-1}$ using equation (5).

## 5. Conclusions

The analysis of three independent sets of data has given parameters that show the optical transitions in $Cr^{3+}$:CYA to be dominated by the non-octahedral contribution to the crystal field. The close agreement in the values of the parameters obtained (table 2) is strong evidence that this conclusion is sound and that variation in the strength of the nephelauxetic

**Table 2.** A summary of the results of calculations of the relative contributions of the non-octahedral and octahedral crystal field components to the R-line broadening as detailed in the subsection indicated.

| Subsection | $\sigma(P_{non})$ | $\sigma(P_{oct})$ |
|---|---|---|
| 4.2.1 | 56 | 20 |
| 4.2.2 | 49 | 25 |
| 4.2.3 | 55 | 15 |

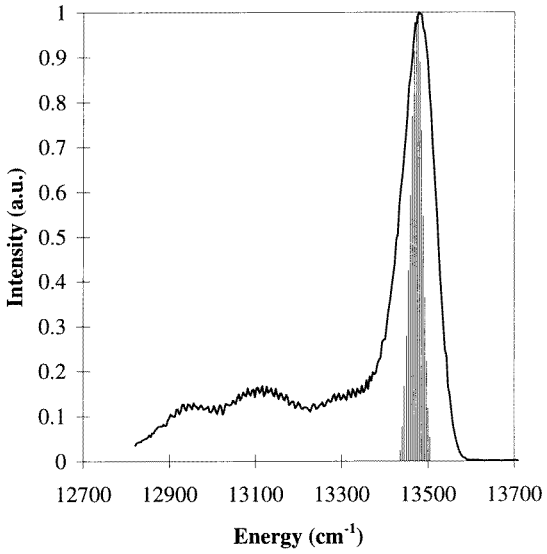


**Figure 13.** The R-line luminescence of CYA excited at 600 nm at 15 K. The histogram represents the density of R-line centre energies excited, calculated by equations (12) and (14). The histogram has been moved to lower energy for comparison with the $R_1$ luminescence.

effect [16] is not required to explain the broadening. The dominance of the non-octahedral contribution is illustrated by figure 13 in which the distribution of centre energies (for the latter calculation) is compared with the fluorescence spectrum obtained when excited at 600 nm. It is clear that the contribution of the variation of the octahedral crystal field makes only a small contribution to the broadening.

Slight deviations between experimental data and the models and between different models are attributed to the mismatch between actual and modelled distributions. In the analysis presented here all distributions are taken to be Gaussian. In fact a superposition of Gaussian distributions, each of which is due to a different combination of $Ca^{2+}$ and $Y^{3+}$ second-nearest neighbours, is likely to be a truer representation. It is highly unlikely that such substitutional disorder will result in perfect Gaussian distributions and this theme is continued in the second paper in this series where electron spin resonance results are presented and discussed [6].

It has been shown that the effect of substitutional disorder on the broadening of optical transitions of $Cr^{3+}$ impurity ions in CYA is principally due to the effect of the variation of the non-octahedral crystal field as has previously been observed in the similarly disordered gallogermanates [9].

**Acknowledgments**

In Japan, this work was supported by a grant-in-aid for scientific research from the Ministry of Education, Science and Culture (07650049). At Strathclyde, the research programme has been funded by joint EPSRC/MOD research grants (GR/F/54105 and GR/H/66143) and the Nuffield Foundation. Travel funds awarded under a joint research programme by the Japanese Society for the Promotion of Science, the Royal Society and the British Council are gratefully achnowledged. Some of the analysis presented in this paper utilized ideas and software developed by Dr Marek Grinberg of the Copernicus University, Torun, Poland.

**References**

[1] Sugano S, Tanabe Y and Kamimura H 1970 *Multiplets of Transition Metal Ions in Crystals* (New York: Academic)
[2] Yamaga M, Yosida T, Naitoh Y and Kodama N 1994 *J. Phys.: Condens. Matter* **6** 4381
[3] Yamaga M, Henderson B, Yosida T, Naitoh Y and Kodama N 1995 *Phys. Rev.* B **51** 3438
[4] Shannon R D, Oswald R A, Parise J B, Chai B H T, Byszowski P, Pajaczow A and Sobolewski R 1992 *J. Solid State Chem.* **98** 90
[5] Yamaga M, Henderson B and O'Donnell K P 1992 *J. Lumin.* **46** 397
[6] Yamaga M, Takeuchi H, Kodama N, Inoue Y, Yosida T, Fukui M, Holliday K and Macfarlane P I in preparation
See also Yamaga M, Takeuchi H, Holliday K, Macfarlane P I, Henderson B, Inoue Y and Kodama N 1995 *Radiat. Eff. Defects Solids* **135** 223
[7] Marshall A, O'Donnell K P, Yamaga M, Henderson B and Cockayne B 1990 *Appl. Phys.* A **50** 565 and references therein
[8] Luci A, Castrignano T, Grassano U M, Casalboni M and Kaminskii A A 1995 *Phys. Rev.* B **51** 1490 and references therein
[9] Grinberg M, Macfarlane P I, Henderson B and Holliday K 1995 *Phys. Rev.* B **52** 3917
[10] Henderson B, Yamaga M, Gao Y and O'Donnell K P 1992 *Phys. Rev.* B **46** 652 and references therein
[11] Monteil A 1990 *J. Phys.: Condens. Matter* **2** 9639
[12] Macfarlane P I 1995 *PhD Thesis* University of Strathclyde
[13] Sutton B D 1968 *Electronic Spectra of Transition Metal Complexes* (New York: McGraw-Hill) p 60
[14] Joergensen C K 1960 *Absorption Spectra and Chemical Bonding in Complexes* (Oxford: Pergamon)
[15] Riesen H and Krausz E 1992 *J. Chem. Phys.* **97** 7902
[16] Macfarlane P I, Holliday K and Henderson B 1996 *Chem. Phys. Lett.* at press
[17] Macfarlane R M 1967 *J. Chem. Phys.* **47** 2066
[18] Owen J and Thornley J H M 1966 *Rep. Prog. Phys.* **29** 675
[19] Henderson B and Wertz H 1977 *Defects in the Alkaline Earth Oxides* (London: Taylor and Francis)
[20] Henderson B and Imbusch G F 1989 *Optical Spectroscopy of Inorganic Solids* (Oxford: Clarendon)